CrossMark

J. Fluid Mech. (2018), *vol.* 855, *pp.* 43–66. © Cambridge University Press 2018
doi:10.1017/jfm.2018.656

Complex dynamics in a stratified lid-driven square cavity flow

Ke Wu[1], **Bruno D. Welfert**[1] **and Juan M. Lopez**[1,†]

[1]School of Mathematical and Statistical Sciences, Arizona State University, Tempe, AZ 85287, USA

(Received 26 March 2018; revised 16 July 2018; accepted 8 August 2018;
first published online 20 September 2018)

The dynamic response to shear of a fluid-filled square cavity with stable temperature stratification is investigated numerically. The shear is imposed by the constant translation of the top lid, and is quantified by the associated Reynolds number. The stratification, quantified by a Richardson number, is imposed by maintaining the temperature of the top lid at a higher constant temperature than that of the bottom, and the side walls are insulating. The Navier–Stokes equations under the Boussinesq approximation are solved, using a pseudospectral approximation, over a wide range of Reynolds and Richardson numbers. Particular attention is paid to the dynamical mechanisms associated with the onset of instability of steady state solutions, and to the complex and rich dynamics occurring beyond.

Key words: internal waves, nonlinear dynamical systems, stratified flows

1. Introduction

The processes by which shear at the surface of a stably stratified body of fluid mixes and deepens the upper portions of the fluid body play an important role in the dynamics of many situations of interest, such as in lakes and oceans as well as in many industrial flows (Turner 1979; Fernando 1991; Stevens & Imberger 1996; Ivey, Winters & Koseff 2008). In general, mixing and turbulence tend to be suppressed when the fluid is sufficiently stably stratified, however when shear stress and buoyancy stratification are roughly in balance, the resultant dynamics can be quite complicated (Sherman, Imberger & Corcos 1978; Majda & Shefter 2000; Peltier & Caulfield 2003).

The situation where an unsteady well-mixed region is separated from a stably stratified region is a common occurrence in many geophysical and astrophysical settings, and there continues to be intense interest in these flows, particularly in regards to the mechanisms by which energy and possibly momentum from the well-mixed region can be transported deep into the stratified region. Internal wave beams are a leading candidate and it is of much interest to understand how these are generated (Michaelian, Maxworthy & Redekopp 2002; Dohan & Sutherland 2003; Pham, Sarkar & Brucker 2009; Ansong & Sutherland 2010; Munroe & Sutherland 2014).

Our understanding of the processes involved is still quite limited. A useful analogue problem that is relatively straightforward to produce as a laboratory experiment and

† Email address for correspondence: juan.m.lopez@asu.edu

https://doi.org/10.1017/jfm.2018.656 Published online by Cambridge University Press

to simulate numerically is the lid-driven stratified cavity flow. Many studies exist in cavities with various aspect ratios or shapes, driven at one or more walls, with a temperature gradient either in the direction opposite to gravity (stable stratification), the perpendicular direction (horizontal convection) or in the same direction (Rayleigh–Bénard convection), in various media (air, water, oils, with different Prandtl numbers Pr), or in the presence of internal obstacles or fins. However, relatively few studies have explored the flow behaviour over a comprehensive range of the Reynolds and Richardson numbers, Re and Ri, characterising the shear and buoyancy of the flow regime. Such a comprehensive study is the goal of the present numerical investigation.

Most studies of the stably stratified configuration used here (where side walls are insulated and the top and bottom walls are kept at fixed temperatures) have been limited to relatively low Grashof numbers, $Gr = Ri\,Re^2 \lesssim O(10^6)$, normally associated (for moderate Pr) with steady state responses (Iwatsu, Hyun & Kuwahara 1993; Nicolás & Bermúdez 2005; Cheng & Liu 2010), in some cases as part of a more general investigation of doubly diffusive (temperature and solute) systems (Maiti, Gupta & Bhattacharyya 2008). The experimental study of Koseff & Street (1985) in a three-dimensional cavity with aspect ratio $1:3:1$ (square vertical cross-section) filled with water ($Pr \approx 7$) remains the quintessential reference for flows at large $Gr \sim O(10^7$–$10^8)$. Their visualisations in the (vertical) symmetry plane provide some general understanding of the competition between shear and buoyancy forces in regimes where the flows are expected to be unsteady, but they only present transient dynamics (the longest experiment corresponds to $t \approx 0.3$ viscous times). Ji, Kim & Hyun (2007) provide experimental and numerical evidence of oscillatory behaviour at large Re and moderate Ri in air ($Pr \approx 0.7$), but they only report on the vertical temperature distribution. Blanchette, Peacock & Cousin (2008) used salt stratification ($Pr \approx 600$) to investigate the relationship between the Péclet number $Pe = Re\,Pr$ and the Rayleigh number $Ra = Gr\,Pr$ at the onset of instability of the steady flow, using the synthetic schlieren technique, at large Ri (with $Gr \sim O(10^{10}$–$10^{12})$) and obtained good agreement with their two-dimensional stability analysis. Cohen *et al.* (2014) investigated stably stratified air flow in experiments in a three-dimensional lid-driven cavity in the large Re and small Ri regime, presenting mean flow features and statistics of the turbulent flow. Consistent with the previous studies, they observed the buoyant confinement of the lid-driven roller to the upper downstream corner. They also presented some scaling analysis of the unsteady flow, but gave few details of the unsteadiness or how it comes about. They found that the flow is not strongly three-dimensional, particularly as the stratification is increased, with the mean kinetic energy in the spanwise flow component being at least ten times weaker than in the streamwise component. This motivates us to do a detailed numerical investigation of the onset and the dynamics of the unsteady flow.

The results of the present study in the two-dimensional square cavity in the low-Re regime ($Re \lesssim 1000$) confirm previous results and observations of steady state solutions and validate our numerical approach. A detailed study of the instability of the steady state as Re is increased is carried out over a large range in Ri. Details of the bifurcating unsteady states are analysed using a bifurcation theoretic approach and frequency analyses of flow kinetic energy, revealing an intricate pattern of responses due to competition between buoyancy and inertial effects.

2. Governing equations

Consider the flow in a rectangular cavity of depth d and width l, filled with a fluid of kinematic viscosity ν, thermal diffusivity κ and coefficient of volume expansion

https://doi.org/10.1017/jfm.2018.656 Published online by Cambridge University Press

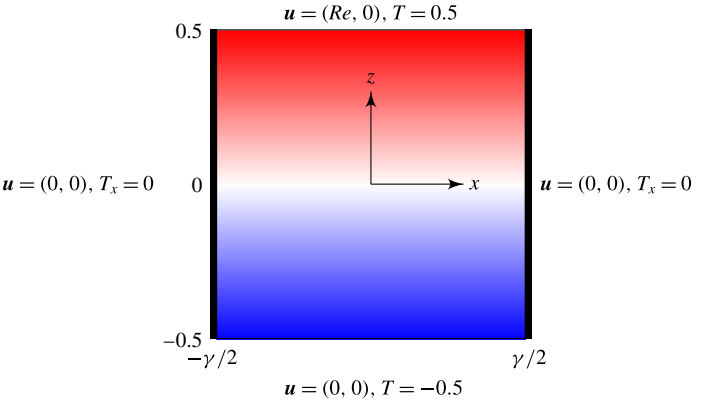


FIGURE 1. (Colour online) Schematic of the system, indicating the non-dimensional coordinate system and boundary conditions. The top boundary moves to the right (positive x direction) at constant speed Re. The colour map shows the linearly stratified temperature distribution (red is $T = 0.5$, blue is $T = -0.5$ and white is $T = 0$) when $Re = 0$.

β. The top boundary of the cavity is driven horizontally at a constant speed U and is maintained at a fixed temperature T_{top}. The bottom boundary is maintained at a cooler fixed temperature T_{bot}, whilst the two side walls are insulated. Gravity g acts in the downward vertical direction. We consider the two-dimensional problem here as it allows for an extensive parameter study. This is also in part motivated by the observation that the dominant modes of linearised instability for stratified shear flows are two-dimensional (Majda & Shefter 1998). The temperature deviation from the mean temperature, $(T_{top} + T_{bot})/2$, is non-dimensionalised with $\Delta T = T_{top} - T_{bot}$. Figure 1 shows a schematic of the system. Using d as the length scale and the viscous time d^2/ν as the time scale, the non-dimensional governing equations, employing the Boussinesq approximation, are

$$\left.\begin{aligned} \boldsymbol{u}_t + \boldsymbol{u}\cdot\boldsymbol{\nabla}\boldsymbol{u} = -\boldsymbol{\nabla}p + \nabla^2\boldsymbol{u} + Gr\,T\boldsymbol{e}_z, \quad \boldsymbol{\nabla}\cdot\boldsymbol{u} = 0, \\ T_t + \boldsymbol{u}\cdot\boldsymbol{\nabla}T = \frac{1}{Pr}\nabla^2 T. \end{aligned}\right\} \tag{2.1}$$

The boundary conditions are:

$$\left.\begin{aligned} \text{top, } (x, z) = (x, 0.5): \quad (u, w, T) = (Re, 0, 0.5), \\ \text{bottom, } (x, z) = (x, -0.5): \quad (u, w, T) = (0, 0, -0.5), \\ \text{sides, } (x, z) = (\pm 0.5\gamma, z): \quad (u, w, T_x) = (0, 0, 0), \end{aligned}\right\} \tag{2.2}$$

where $\gamma = l/d$ is the aspect ratio.

There are four time scales of relevance; these are

$$\left.\begin{aligned} \text{viscous time} \quad \tau_v = d^2/\nu, \\ \text{thermal diffusion time} \quad \tau_\kappa = d^2/\kappa, \\ \text{inertial time} \quad \tau_i = d/U, \\ \text{buoyancy time} \quad \tau_b = \sqrt{d/g\beta\Delta T}. \end{aligned}\right\} \tag{2.3}$$

https://doi.org/10.1017/jfm.2018.656 Published online by Cambridge University Press

The governing parameters can be expressed as ratios of these time scales:

$$\left.\begin{array}{rr} \text{Prandtl number} & Pr = \tau_\kappa/\tau_\nu = \nu/\kappa, \\ \text{Reynolds number} & Re = \tau_\nu/\tau_i = Ud/\nu, \\ \text{Richardson number} & Ri = (\tau_i/\tau_b)^2 = g\beta\Delta Td/U^2, \\ \text{Grashof number} & Gr = (\tau_\nu/\tau_b)^2 = RiRe^2 = \beta g d^3\Delta T/\nu^2. \end{array}\right\} \tag{2.4}$$

In this study $\gamma = 1$ and $Pr = 1$, and we consider variations in the independent parameters Re and Ri.

3. Numerical method

The governing equations (2.1) are discretised using a spectral-collocation method in both spatial directions. Both velocity components and pressure are approximated by Chebyshev polynomials of the first kind with degree less than M, associated with the Chebyshev–Gauss–Lobatto grid. Spatial differentiation is performed via direct matrix-vector multiplication by the pseudo-spectral differentiation matrix.

The boundary condition for the x-velocity at the moving top wall, $u(x, 0.5) = Re$, is discontinuous where it meets the two vertical side walls, which can lead to Gibbs phenomena when using a global spectral method. In order to resolve this numerical issue, we regularise the top wall boundary condition by using:

$$u(x, 0.5) = Re[1 - \exp(-(1 - 4x^2)/\delta)]. \tag{3.1}$$

The small positive number δ controls the distance over which the discontinuity is regularised. For the results presented here, we have used $\delta = 0.03$. Smaller values of δ, corresponding to narrower gaps between the top lid and the vertical sides, lead to qualitatively similar results while significantly increasing the computational demand.

For the smaller Re and Ri values considered, a collocation grid with $M = 128$ points in each direction provides sufficiently many points in the regularisation regions near the top corners to yield reliable results. For larger Re and Ri, finer grids were used, with $M = 196$ being used for the largest Re and Ri in order to resolve the flows.

The time integration scheme used is the fractional-step improved projection method of Hugues & Randriamampianina (1998), based on a linearly implicit and stiffly stable second-order accurate scheme, combining a backward differentiation formula for the linear terms and an implicit mix, equivalent to linear extrapolation, of Adams–Moulton and Adams–Bashforth steps for the nonlinear advective terms (Vanel, Peyret & Bontoux 1986). The predictor stage of the fractional step method solves a Helmholtz equation for a pressure field, for which Neumann conditions consistent with (2.1) are applied at the walls. The corrector stage then projects the resulting predicted velocity field onto the space of (discretely) divergence-free polynomials via a Stokes problem, which is also handled by solving a Helmholtz equation for the corrected pressure, albeit with homogeneous Neumann boundary conditions. The code used in the present study is essentially the same as that used in Lopez *et al.* (2017), but restricted to two-dimensional flow, and augmented with the temperature equation and the buoyancy term in the momentum equation.

Depending on the values of Re and Ri, one or multiple solutions can be obtained from different initial conditions, such as steady state (S), limit cycles (L) or quasi-periodic states (QP) which are mixed modes of limit cycles whose frequencies may or may not be commensurate, and in some parameter regimes even more temporally complicated states exist. In general, the initial condition used is the static

https://doi.org/10.1017/jfm.2018.656 Published online by Cambridge University Press

linearly stratified state, i.e. $u = w = 0$ and $T = z$. Other solutions can be obtained via continuation using solutions from nearby parameter values as initial conditions. To determine the type of solution, we monitor two global indicators of the flow: the non-dimensional heat flux through the bottom wall of the cavity (Nusselt number)

$$Nu = \int_{x=-0.5}^{x=0.5} T_z(x, -0.5)\,\mathrm{d}x, \tag{3.2}$$

and the total kinetic energy

$$E = \frac{1}{Re^2} \int_{z=-0.5}^{z=0.5} \int_{x=-0.5}^{x=0.5} (u^2 + w^2)\,\mathrm{d}x\,\mathrm{d}z. \tag{3.3}$$

In general, $Nu \geqslant 1$ (with $Nu = 1$ for the static state, which only exists at $Re = 0$), and $E < 1$. Note that for steady states, Nu also corresponds to the heat flux through the top boundary, whereas for unsteady states, the heat flux through the top and the bottom are not necessarily the same at any instant in time, but their long-time averages converge to the same value.

Unsteady flows are characterised by their temporal frequencies, f, obtained from the power spectral density (PSD) of the time series (which is first trimmed, de-trended, and Blackman filtered) of the kinetic energy E. Since the flows are computed using the viscous time scale, the frequencies can vary widely with Re and Ri. In order to compare values of f over a large range of Re and Ri, we use the scaled angular frequency

$$F = \frac{f}{\sqrt{Re^2 + Gr}} = \frac{f}{Re\sqrt{1 + Ri}}. \tag{3.4}$$

This scaling reduces the measure f in the viscous time scale to the measure F of the frequency in the inertial time scale when $Gr = 0$ with $Re \neq 0$ fixed (i.e. $Ri = 0$) and to the measure F in the buoyancy time scale when $Re = 0$ with $Gr \neq 0$ fixed (i.e. $Ri \to \infty$), thus providing a smooth transition between these time scales for intermediate Ri values. Plots of the PSDs obtained for fixed Re but different Ri are normalised using the global peak power to reflect relative signal strengths, with the colour scale ranging from white (-50 dB, corresponding to 10^{-5} power) to black (0 dB, associated with unit peak power).

4. Results

Figure 2 provides a global overview of the regions in the (Ri, Re) parameter space where either the steady base state S is the only observed response (unshaded region), or sustained unsteady responses are observed (shaded regions). For fixed Ri, S is observed at low Re, for which viscous effects are dominant. At larger Re, competing shear and buoyancy effects destabilise S and lead to various time-dependent states. In the following subsections, we describe the bifurcations that result in these unsteady states and their nonlinear dynamics.

4.1. *Steady state at low Re numbers*

For small enough Re, the flow evolves to a steady state S for all values of Ri. Figure 3 show streamlines and temperature contours of S for $Ri = 0.05$, 0.5 and 5 at $Re = 1000$. The streamlines are the isocontours of the streamfunction ψ, where $(u, w) = (\psi_z, -\psi_x)$.

https://doi.org/10.1017/jfm.2018.656 Published online by Cambridge University Press

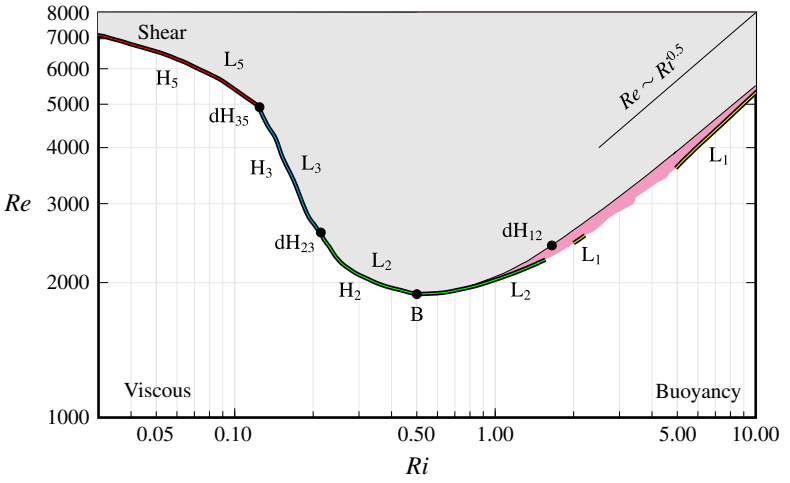


FIGURE 2. (Colour online) Phase diagram in the (Ri, Re) parameter space. Below the Hopf bifurcation curves, H_i with $i = 2$, 3 and 5, only the steady state, S, exists and is stable. Above the Hopf bifurcation curves, unsteady states including the limit cycles L_i with $i = 1$, 2, 3 and 5, exist in the grey shaded region. The dynamics in the magenta shaded region is hysteretic, with S and unsteady states attracting. Codimension-two points where two different Hopf bifurcation curves meet are indicated with bullets for the double-Hopf points dH_{35}, dH_{23} and dH_{12}, as well as the Bautin point B where the Hopf bifurcation H_2 changes from being supercritical to subcritical.

The horizontal temperature gradient T_x, which is a source of vorticity, provides all the essential information on the dynamics of the flow and is also included in figure 3; it will be the main quantity of interest at higher Re values.

For $Ri \ll 0.5$, shear effects dominate over buoyancy effects, resulting in full vertical penetration of the lid-driven roller and temperature homogenisation throughout most of the cavity. This leads to a steep temperature gradient at the bottom of the cavity (see figure 3*a* for $Ri = 0.05$). The presence of two weak secondary recirculation zones at the bottom corners is consistent with the flow in the isothermal lid-driven cavity (Koseff & Street 1985; Iwatsu *et al.* 1993; Nicolás & Bermúdez 2005). The impact of the non-isothermal conditions is that in the core of the main roller, the temperature is essentially uniformly hot and it is inside this roller where the streamfunction has non-zero gradients (i.e. there is a meridional circulation). The lid-driven roller is delineated by regions of large horizontal temperature gradients T_x separating the isothermal overturning flow in the roller from the temperature-stratified near-static fluid outside the roller.

For $Ri \approx 0.5$, buoyancy and shear effects are of comparable strength and their competition results in a smaller roller restricted toward the downstream top corner and a deeper stratification zone in the bottom of the cavity (see figure 3*b* for $Ri = 0.5$). Since advection brings the temperature at the top of the stratification zone in line with the temperature at the top of the cavity, the temperature gradient through the bottom stratified region is lower than it is at smaller Ri. These features are consistent with the numerical results in Iwatsu *et al.* (1993).

For $Ri \gg 0.5$, buoyancy confines the roller to the upper right corner of the cavity, and the flow is essentially unable to penetrate into the stratified zone. The streamlines indicate a number of very weak horizontal recirculation layers in the stratified zone.

https://doi.org/10.1017/jfm.2018.656 Published online by Cambridge University Press

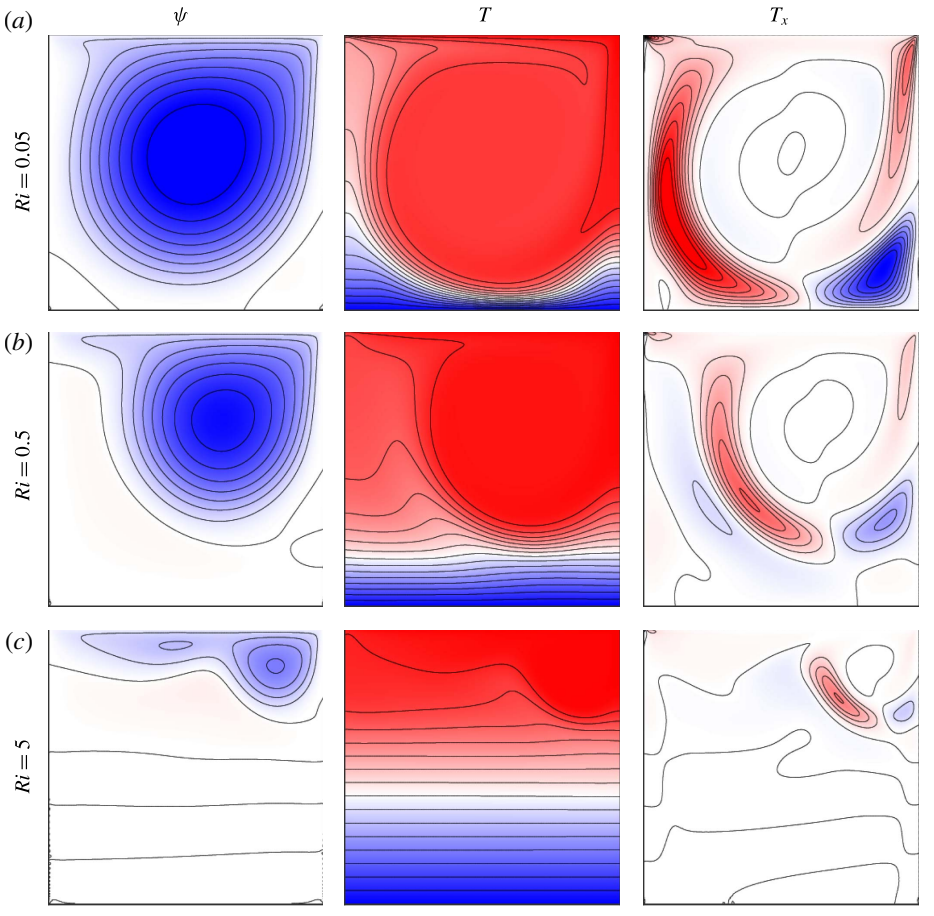


FIGURE 3. (Colour online) Streamlines ψ, isotherms T and horizontal temperature gradient T_x of S at $Re = 1000$ and Ri as indicated. The contour levels are equispaced in ranges $|\psi| \leqslant 100$, $|T| \leqslant 0.5$, and $|T_x| \leqslant 1.5$.

In the example shown in figure 3(*c*) for $Ri = 5$, there are four such layers. For different Re and Ri, different numbers of similar layers have been reported (Koseff & Street 1985; Nicolás & Bermúdez 2005).

The radius of the lid-driven roller can be estimated from the vertical position z_ψ of the minimum of the streamfunction ψ, by assuming a perfectly circular roller, namely $R_\psi \approx 0.5 - z_\psi$. Alternately, the radius can be estimated from $Nu \approx 1/(1 - 2R_{Nu})$ by assuming a constant vertical temperature gradient below a roller of radius R_{Nu} and a uniform temperature within the roller. These assumptions are supported by figure 3(*b*). The two estimates of the radius, R_ψ and R_{Nu}, are shown in figure 4 for $Re = 1000$ and $Ri \in [0.01, 10]$. The two roller radii estimates are similar, especially for $Ri \lesssim 0.5$. Both estimates decrease with increasing Ri for $Ri \gtrsim 0.2$, with the roller depth $2R_\psi$ or $2R_{Nu}$ being approximately two thirds the depth of the cavity at $Ri = 0.5$, and one half at $Ri = 1$. These results are also qualitatively similar to those measured experimentally by Cohen *et al.* (2014, figure 6).

https://doi.org/10.1017/jfm.2018.656 Published online by Cambridge University Press

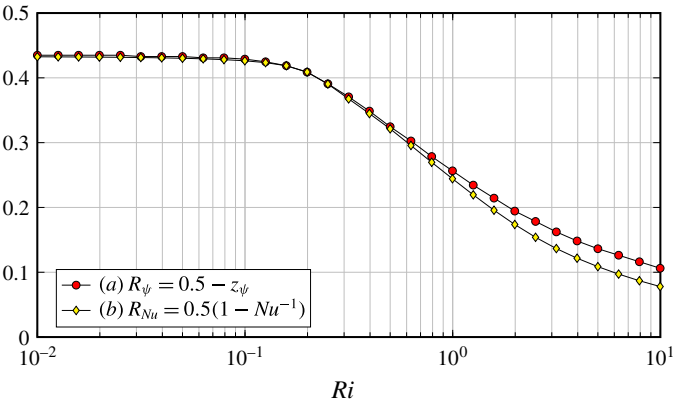


FIGURE 4. (Colour online) Radius of the primary roller as a function of Ri at $Re = 1000$, estimated from the vertical position z_ψ of the streamfunction minimum, and the Nusselt number Nu.

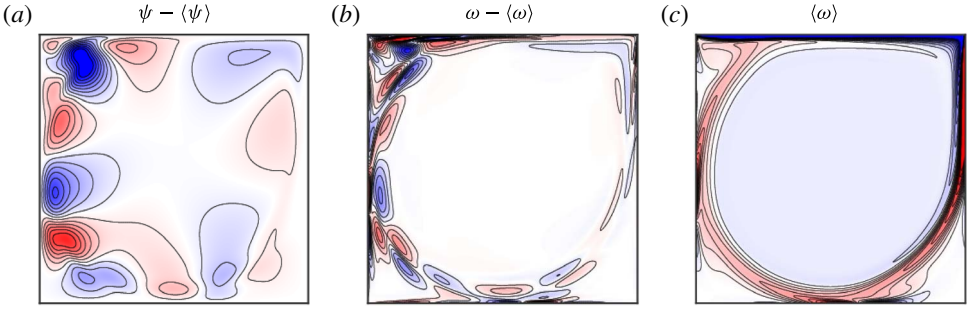


FIGURE 5. (Colour online) Snapshots of the deviations from the time averages of (*a*) the streamfunction, (*b*) vorticity and (*c*) the time-averaged vorticity, for the limit cycle L_5 at $Re = 8016$ and $Ri = 0$.

4.2. *Instability of S for $Ri < 0.5$: supercritical Hopf bifurcations*

For $Ri < 0.5$, the steady state S loses stability as Re is increased beyond a critical value via supercritical Hopf bifurcations, resulting in time periodic flows. At $Ri = 0$, oscillations appear at the critical $Re \approx 8016$ (using a 128×128 Chebyshev grid), which compares well with values in Brezillon, Girault & Cadou (2010, table 3) obtained using various different numerical approaches and top-corner velocity regularisations. Figure 5 shows snapshots of the deviations from the time averages of the streamfunction and the vorticity, $\psi - \langle\psi\rangle$ and $\omega - \langle\omega\rangle$, as well as the time-averaged vorticity, $\langle\omega\rangle$. The deviation from the mean streamfunction is comprised of 5 negative cells interlaced with 5 positive cells which propagate around the periphery of the roller in the clockwise direction. This $m = 5$ cycle is denoted L_5. The structure of L_5 is similar to that of the real and imaginary parts of the critical Hopf eigenmode reported in Brezillon *et al.* (2010, figure 8), Poliashenko & Aidun (1995, figure 2), Fortin *et al.* (1997, figure 5) and Auteri, Parolini & Quartapelle (2002, figure 14). The scaled angular frequency of L_5 is $F \approx 0.45$, which matches the frequency values reported in Brezillon *et al.* (2010, table 3). This frequency corresponds to the rate at which a cell replaces the next cell of the same sign.

https://doi.org/10.1017/jfm.2018.656 Published online by Cambridge University Press

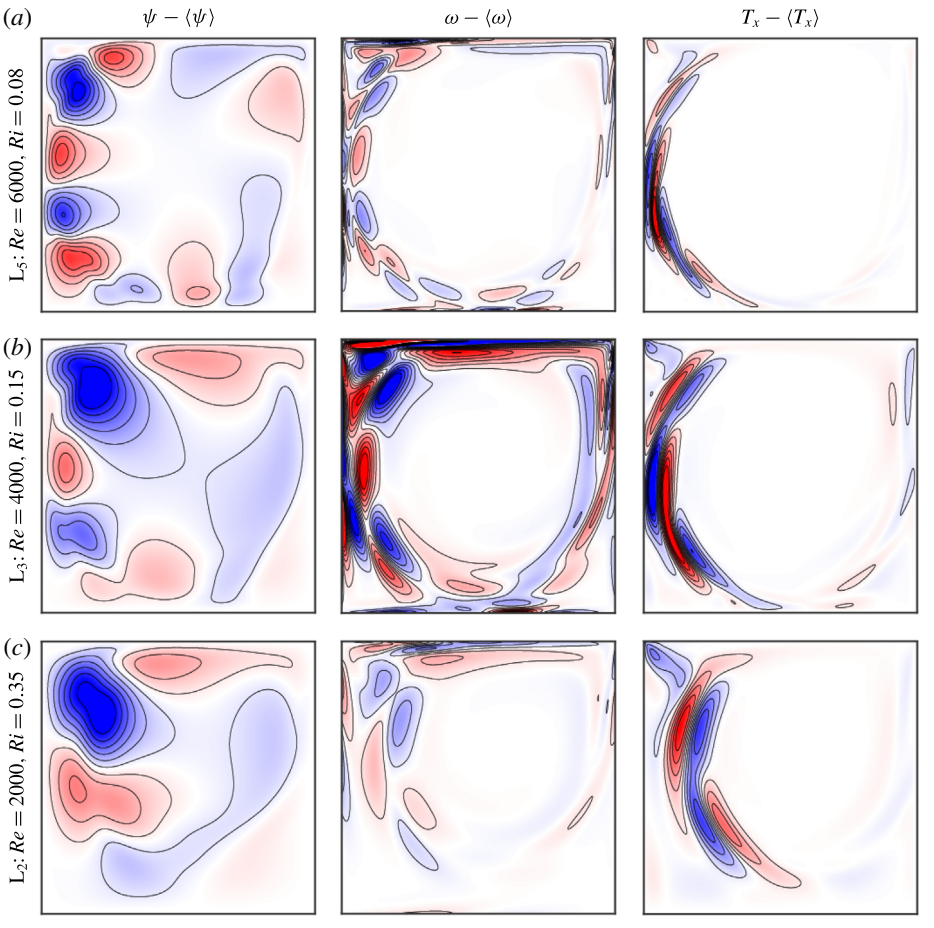


FIGURE 6. (Colour online) Snapshots of deviations from their time averages for streamfunction, vorticity and horizontal temperature gradient, for the limit cycles at parameter points (Re, Ri) as indicated. Supplementary movie 1, available at https://doi.org/10.1017/jfm.2018.656, shows animations of $\psi - \langle\psi\rangle$ for each limit cycle over one period.

Consequently, $F/m \approx 0.09$ is the fundamental frequency associated with a complete rotation of a given cell around the roller.

As Ri increases from 0, the critical Re decreases. The curve in (Ri, Re)-space along which S loses stability is made up of three distinct Hopf bifurcation curves H_m, with $m = 5$, 3 and 2 associated with three different limit cycles L_m. Figure 6 illustrates the streamfunction, vorticity and horizontal temperature gradient deviations from their time averages for L_5, L_3 and L_2, computed at Re slightly above critical for $Ri = 0.08$, 0.15 and 0.35. Movies of $\psi - \langle\psi\rangle$ for the three limit cycles over one period are available in supplementary movie 1. The streamfunction deviations of L_m show m pairs of interlacing negative and positive cells. While it may be difficult to count the number of cell pairs from a single snapshot due to their elongation at the windward vertical wall, the animations in movie 1 make this task much easier as the cells propagate around the periphery of the roller. The structure of L_5 at $Ri = 0.08$ is essentially the same as that of L_5 at $Ri = 0$ in figure 5. The cells thicken as their number $2m$ becomes

https://doi.org/10.1017/jfm.2018.656 Published online by Cambridge University Press

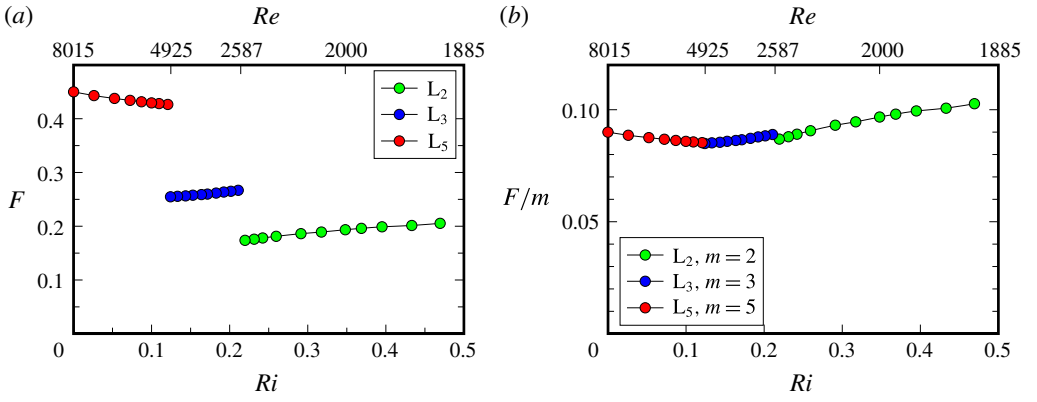


FIGURE 7. (Colour online) (*a*) Scaled frequencies F of the limit cycles L_2, L_3 and L_5 at Ri and Re slightly beyond the supercritical Hopf bifurcations shown in figure 2, and (*b*) the corresponding scaled frequencies F/m.

smaller in different regions of (Ri, Re)-space. The frequencies of the limit cycles at the bifurcation are shown in figure 7. For smaller m, the larger cell size of L_m leads to a lower scaled angular frequency F, but the rotation number F/m exhibits little variation along the three Hopf bifurcation curves, and is almost continuous across modal transitions.

The Hopf curves intersect each other at double-Hopf bifurcation points. There are two of these for $Ri < 0.5$: dH_{23} at (Ri, Re) $\approx$ (0.214, 2587) and dH_{35} at (Ri, Re) $\approx$ (0.1245, 4925). Typically, in the neighbourhood of a double-Hopf point, a quasi-periodic mixed mode of the two limit cycles involved also exists, and in some cases the mixed modes is stable (Kuznetsov 2004). This is the case here for the two double-Hopf bifurcations, as shown in figure 8. The mixed modes M_{23} and M_{35} are essentially superpositions of the limit cycles L_2 and L_3, and L_3 and L_5, respectively, and are stable in parameter regimes emerging from the double-Hopf points. In the regions where the mixed modes are stable, the limit cycles are not. The boundaries separating the parameter regions where the mixed mode is stable and the two regions where the limit cycles are stable are curves of Neimark–Sacker bifurcations. The slopes of these curves and of the Hopf bifurcations curves very close to the double-Hopf point provide estimates of the normal-form coefficients of the two double-Hopf bifurcations. From these, one can determine the nonlinear behaviour of the flow states. In the classification of Kuznetsov (2004, § 8.6), dH_{35} is simple type II, while the approximate alignment of the Hopf curve H_3 with a Neimark–Sacker curve prevents the distinction between simple type II or simple type III for dH_{23} (Kuznetsov 2004, figure 8.25). Nevertheless, both simple type II and simple type III double-Hopf bifurcations are cases with the mixed mode being stable.

4.3. *Instability of S for $Ri > 0.5$: subcritical Hopf bifurcations*

For $Ri \gtrsim 0.5$, the steady state S loses stability as Re increases via a subcritical Hopf bifurcation. The Bautin point B at which the Hopf bifurcation H_2 switches from being supercritical to subcritical is at (Ri, Re) $\approx$ (0.5, 1885). At this point a cyclic-fold (saddle-node bifurcation of limit cycles) bifurcation curve also emerges, along which the unstable limit cycle L_2 created at the subcritical H_2 bifurcation

https://doi.org/10.1017/jfm.2018.656 Published online by Cambridge University Press

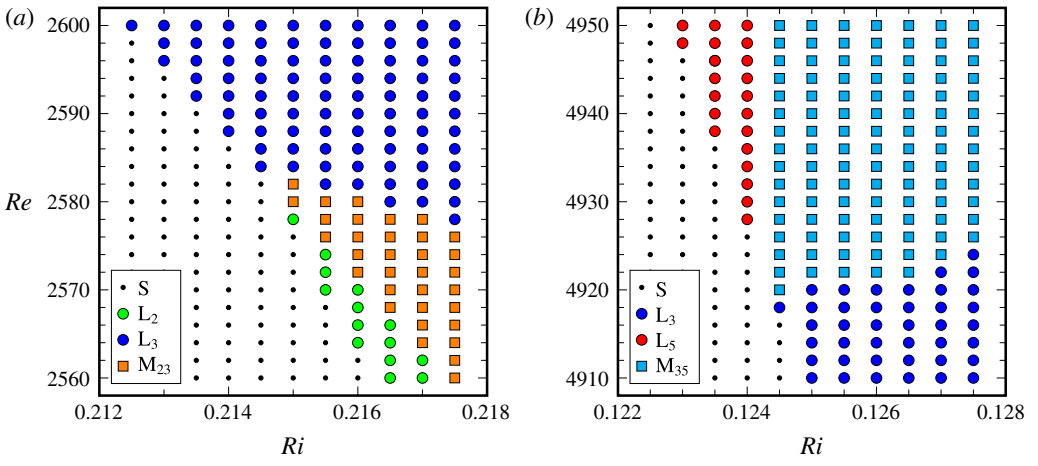


FIGURE 8. (Colour online) Stable states observed via continuation of the steady state by increasing *Ri* at fixed *Re* in the indicated parameter ranges. The presence of two stable limit cycle solutions and a stable (quasi-periodic) mixed state indicate the presence of two supercritical Hopf branches intersecting at double-Hopf points corresponding to (*a*) dH_{23} and (*b*) dH_{35}.

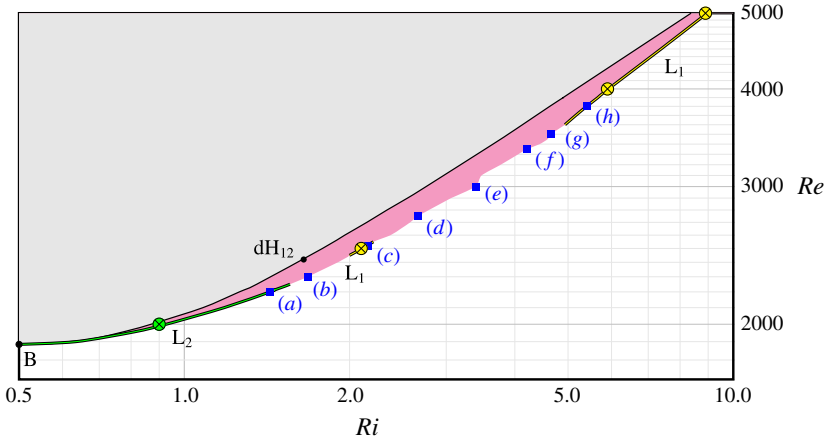


FIGURE 9. (Colour online) Close up from figure 2 of the hysteresis region (shaded magenta) starting from the Bautin point B, between the subcritical Hopf curve where the steady state loses stability and the cyclic-fold curve. The ⊗ symbols indicate the locations in (*Re*, *Ri*) space where examples of limit cycles L_2 and L_1 are shown in figure 10. Time series of *E* and phase portraits of sample states at the edge of the hysteresis region indicated by the blue squares labelled (*a–h*) are shown in figure 11.

(the lower branch cycle) becomes stable (upper branch cycle) as it is folded back in parameter space (Kuznetsov 2004). Both S and upper branch L_2 co-exist and are stable, and lower branch L_2 is unstable in the hysteresis region between the subcritical Hopf and cyclic-fold curves, the region shaded magenta in figure 2; also see the close-up version in figure 9 where the cyclic-fold curve of L_2 is drawn as a thick green curve on the high-*Ri*/low-*Re* edge of the hysteresis region. This cyclic-fold

https://doi.org/10.1017/jfm.2018.656 Published online by Cambridge University Press

curve which starts at the Bautin point B ends at $(Ri, Re) \approx (1.56, 2250)$. Beyond this point, the upper branch state is a quasi-periodic state all the way to the edge of the hysteresis region. Then, at the edge of the hysteresis region at $(Ri, Re) \approx (2, 2450)$, the edge is once again a cyclic-fold bifurcation, but now involving a limit cycle L_1. The extent of this cyclic-fold curve is drawn as a thick yellow line in figure 9. The frequencies of L_1 and L_2 on the upper branches of the respective cyclic-fold bifurcations are very close to a 1 : 2 frequency ratio, and the spectral signature of the quasi-periodic state has all linear combinations of these two frequencies. This behaviour is indicative of an underlying double-Hopf bifurcation dH_{12}, where both Hopf bifurcations from the steady state S are subcritical. This codimension-two point is estimated to be at $(Ri, Re) \approx (1.65, 2420)$, indicated in the phase diagram figure 2, as well as in figure 9. This type of double-Hopf bifurcation is strongly resonant and in its neighbourhood, homoclinic and heteroclinic dynamics and transverse intersections of stable and unstable manifolds are to be expected, leading to slow–fast dynamics and chaotic behaviour. This complex dynamics is associated with the phase of the limit cycles not decoupling from their amplitude, opening up the possibility for the phases of the two limit cycles to lock and unlock via heteroclinic bifurcations (Knobloch & Proctor 1988). The cyclic-fold curve of L_1 is short, extending only to $(Ri, Re) \approx (2.2, 2550)$, beyond which the upper branch states at the edge of the hysteresis region are quasi-periodic or more complex (some are described below). Further along the edge, from $(Ri, Re) \approx (5, 3600)$ to at least $(Ri, Re) \approx (9, 5000)$, the edge is once again demarcated by a cyclic-fold curve of L_1 (also drawn as a thick yellow line in figure 9).

Figure 10 shows snapshots of the streamfunction, vorticity and horizontal temperature gradient deviations from their time averages for the limit cycles L_1 and L_2 near the cyclic-fold bifurcation curves described above, at (Ri, Re) points indicated as $\otimes$ in figure 9. For L_2 at $(Ri, Re) = (0.9, 2000)$, the two cells of each sign in the streamfunction deviation (blue and red) are easily recognisable, and to a lesser extent in the vorticity and horizontal temperature gradient deviations. At this relatively small Ri, the lid-driven roller occupies most of the cavity. At larger Re and Ri, L_1 with a large single pair of cells in the streamfunction deviation is the state undergoing the cyclic-fold bifurcation. At these larger Ri, the roller is more confined to the downstream top corner region and the lower part of the cavity is nearly linearly stratified. The ratio of the L_1 frequency and the local buoyancy frequency in the lower part of the cavity is such that internal wave beams are emitted from the oscillatory roller into the stratified region at an angle of approximately 45° such that they reflect back from lower left corner of the cavity. This retracing of the beam leads to enhanced phase coherence. Supplementary movie 2 shows $T_x - \langle T_x \rangle$ for the four cases in figure 10, each animated over one period. In the movie, it is evident that, even for the L_2 case with the relatively small Ri, there is a hint of a wave beam also retracing off the lower left corner. The energy of the wave beams does not exceed a few per cent of the total energy.

Between $(Ri, Re) \approx (2.2, 2550)$ and $(Ri, Re) \approx (5, 3600)$, the last state observed on the upper branch of the hysteresis region before falling back to the steady state as Ri is increased is a quasi-periodic (QP) state with strong L_1 content. A pure L_1 is also observed slightly below $(Ri, Re) \approx (5, 3600)$, suggesting a subcritical bifurcation along the fold between the QP and L_1 states.

Figure 11 illustrates specific responses obtained along the upper branch, at the last stable time-dependent state obtained when increasing Ri, labelled $(a–h)$ in figure 9. The plots show the time series $E(t)$ over 0.25 viscous time units as well as phase

https://doi.org/10.1017/jfm.2018.656 Published online by Cambridge University Press

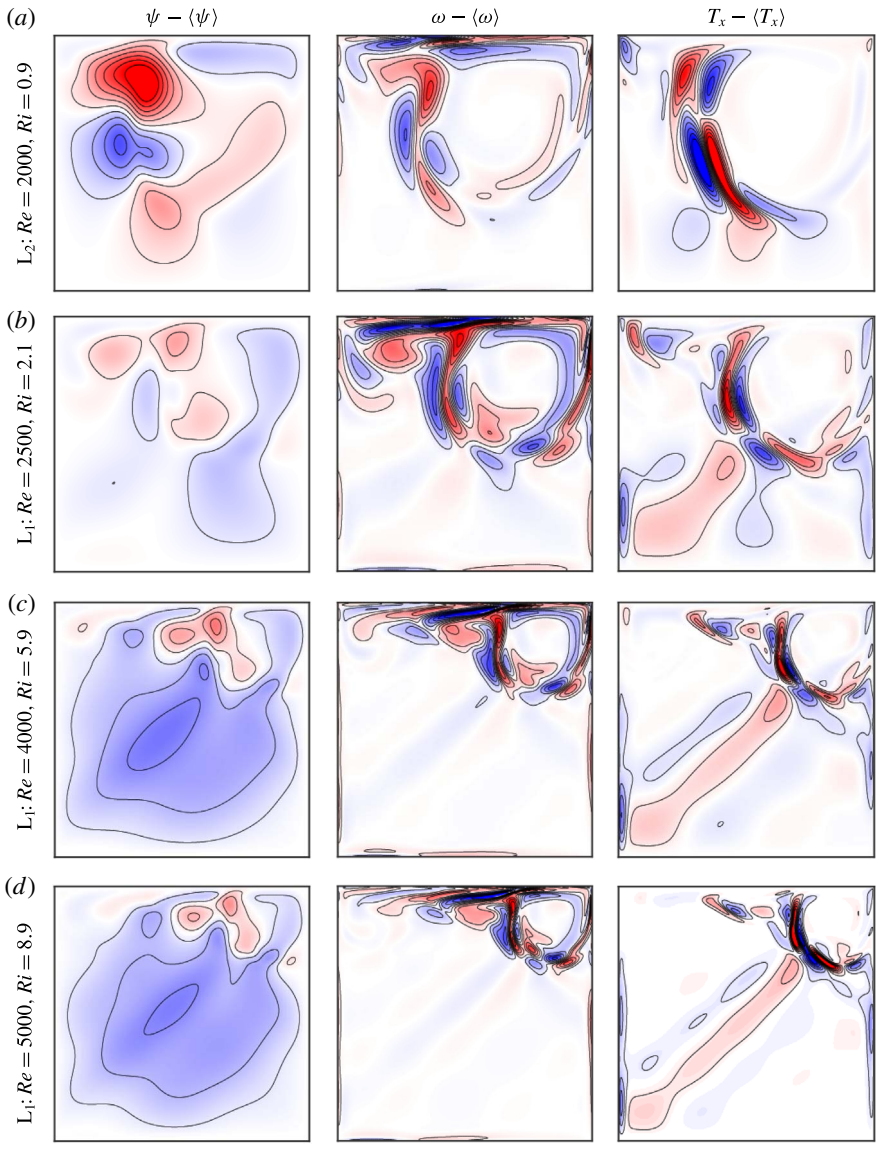


FIGURE 10. (Colour online) Snapshots of deviations from their time averages for streamfunction, vorticity and horizontal temperature gradient, for the limit cycles at parameter points (Re, Ri) as indicated. Supplementary movie 2 shows animations of $T_x - \langle T_x\rangle$ for over one period.

portraits obtained by plotting $E(t)$ against a delayed $E(t-\tau)$. The delay τ was selected such that the associated frequency $F = 1/(\tau Re\sqrt{1+Ri}) = 0.3$ is larger, but not excessively so, than the scaled frequency $F \approx 0.2$ of L_2. The responses (*a*) and (*c*) correspond to limit cycles L_2 and L_1 respectively. Limit cycle L_1 is also the response in (*h*), and its presence can be recognised in the quasi-periodic responses (*e*,*f*,*g*), with the low beat frequency and the frequency of L_1 locked in a 1 : 18 ratio in case (*e*). Case (*b*) illustrates a locked mixed mode of L_1 and L_2 in a regime close to the

https://doi.org/10.1017/jfm.2018.656 Published online by Cambridge University Press

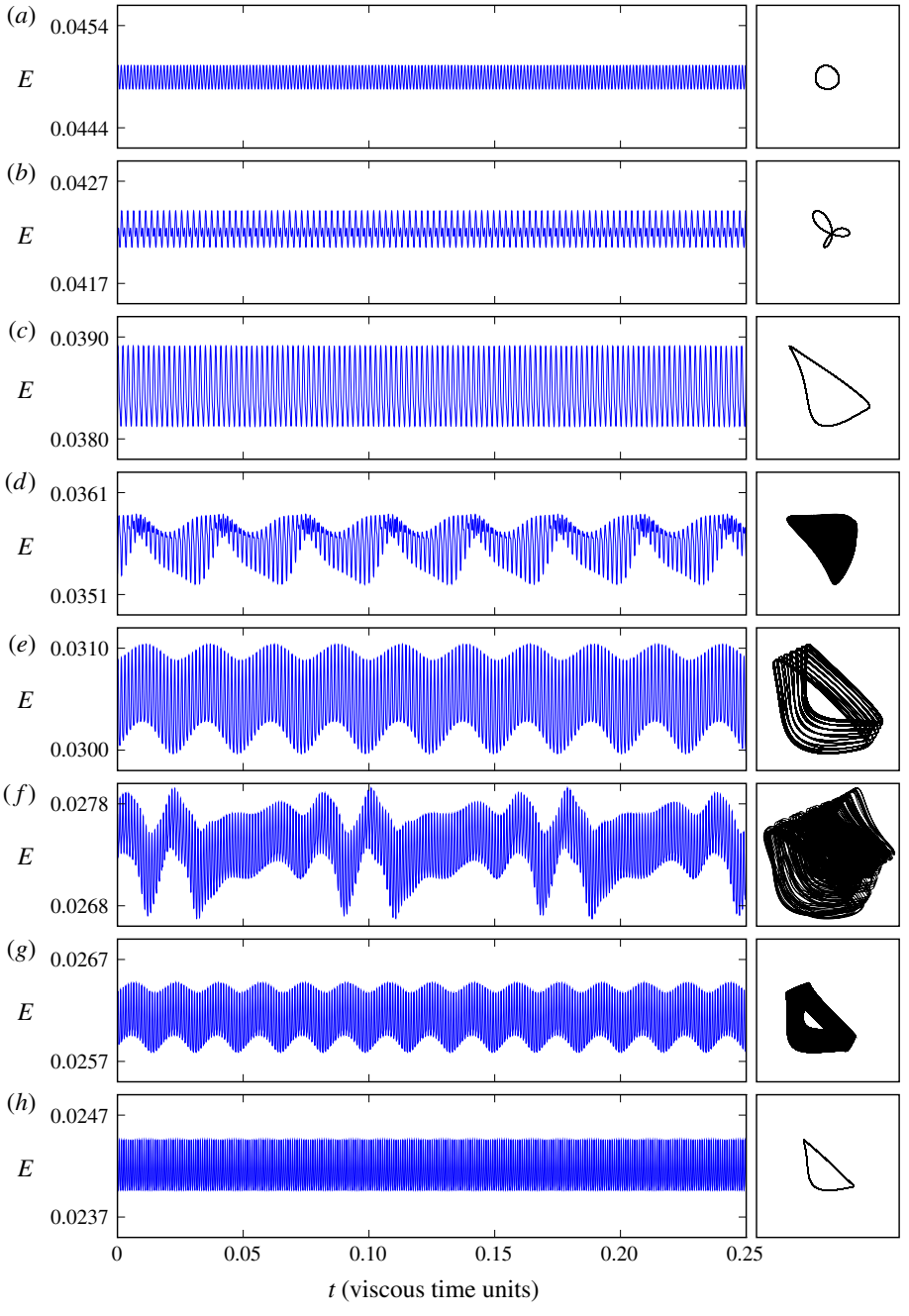


FIGURE 11. (Colour online) Time series of the E responses over a window of 0.25 viscous units, at the (Ri, Re) values indicated in figure 9 by the locations of the labels $(a–h)$, together with the corresponding phase portraits using $(E(t-\tau), E(t))$ with delay $\tau = 1/(0.3Re\sqrt{1+Ri})$.

double-Hopf point dH_{12}. This mixed mode seems to arise from a flip bifurcation of L_2 (Floquet multiplier crossing the unit circle at -1) at a lower Ri (or Re). Response (d) exhibits near heteroclinic behaviour between limit cycles L_1 and L_2, with about

https://doi.org/10.1017/jfm.2018.656 Published online by Cambridge University Press

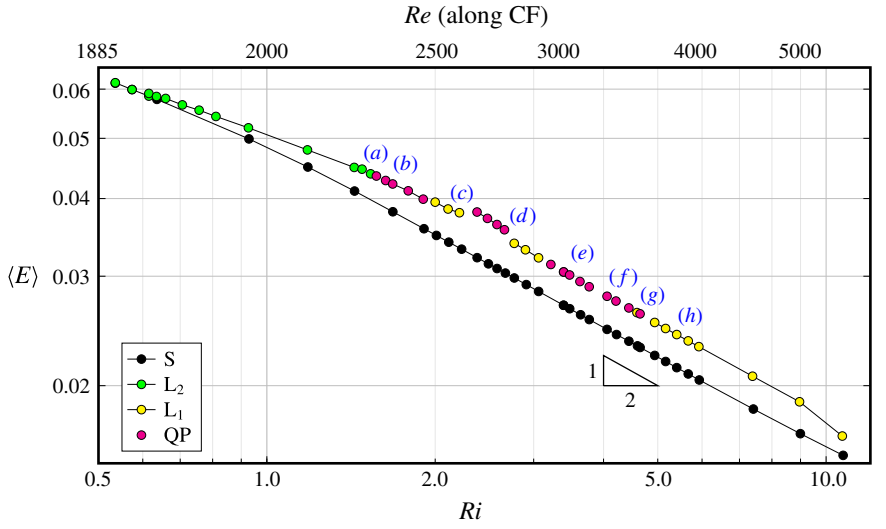


FIGURE 12. (Colour online) Scaled kinetic energy E of steady states and mean time scaled kinetic energy $\langle E\rangle$ of unsteady states along the cyclic-fold upper branch as functions of Ri. The points labelled (*a–h*) correspond to the same labelled points in figure 9.

equal power at both frequencies, again likely associated with the strongly resonant double-Hopf bifurcation H_{12}. A plot of the (long) time average of the scaled kinetic energy $\langle E\rangle$ along the upper branch of the fold in figure 12 shows that the mixed mode in case (*d*) has slightly higher kinetic energy than its L_1 neighbours.

The scaling $Re \sim \sqrt{Ri}$ holds along the subcritical Hopf curve (black line in figure 2). This scaling can be justified near the onset of instability of the base steady state S at large Ri and Re by assuming a linear stratification, so that

$$\boldsymbol{u} = (u(z,t), w(x,t)), \quad p = p(x,t), \quad T_x = T_{zz} = 0. \tag{4.1a–c}$$

In this case, the system (2.1) simplifies to

$$u_t + wu_z = -p_x + u_{zz}, \quad w_t + uw_x = w_{xx} + Gr\,T, \quad T_t + wT_z = T_{xx}/Pr. \tag{4.2a–c}$$

In the steady case, this further reduces to

$$w_{xxxx} = uw_{xxx} - Gr\,T_{xx} = uw_{xxx} - r^4 w, \tag{4.3}$$

where $r^4 = T_z GrPr$. The existence of a similarity solution $w = w(rx)$ leads to the condition $u \sim r$, i.e. $Re \sim r \sim \sqrt[4]{Gr}$ using the entrainment condition $u = -Re$ at the top of the stratified region. Similar arguments for a related problem are made in Hanratty, Rosen & Kabel (1958), and in Blanchette *et al.* (2008) who also present supporting physical experiments.

In the time-dependent case, balancing the terms in (4.2) and assuming the solution to be periodic with angular frequency ω yields

$$\omega^2 w \sim w_{tt} \sim Gr\ T_t \sim Gr\ T_z w, \tag{4.4}$$

https://doi.org/10.1017/jfm.2018.656 Published online by Cambridge University Press

Re	1900	2000	2100	2200	2500	3000	3500	4000	5000	6000
Peak power	0.087	0.12	0.43	0.70	1.6	2.5	2.1	2.7	3.5	3.4
Ri at peak	0.581	0.615	0.512	0.652	0.548	0.542	0.714	0.622	0.652	0.555

TABLE 1. Peak power and corresponding *Ri* of *E* spectral data at *Re* as indicated.

i.e. $\omega \sim \sqrt{Gr\ T_z}$. So, for large *Ri*,

$$F \sim \frac{\omega/2\pi}{Re\sqrt{Ri}} = \frac{\omega/2\pi}{\sqrt{Gr}} \sim \frac{\sqrt{T_z}}{2\pi} \sim \frac{1}{2\pi} \approx 0.159, \tag{4.5}$$

approaches a constant, further justifying the choice of the frequency scaling (3.4).

The data in figure 12 also suggest the scaling

$$\langle E \rangle \sim 1/\sqrt{Ri} \sim 1/Re \sim 1/\sqrt[4]{Gr}, \tag{4.6}$$

along the fold curves. There, the peak frequency f of the response scales like

$$f = F\,Re\sqrt{1+Ri} \sim Re\sqrt{Ri} \sim Ri, \tag{4.7}$$

resulting in $\langle E \rangle \sim 1/\sqrt{f}$.

The scaled frequency of L_1 along its fold above $(Ri, Re) \approx (5, 3600)$ was observed to marginally increase from $F \approx 0.115$ to $F \approx 0.118$ at $(Ri, Re) \approx (9, 5000)$. However, at $(Ri, Re) \approx (10.7, 5500)$ (corresponding to the rightmost upper data point in figure 12) the scaled frequency F of L_1 at its fold was found to be significantly higher, namely $F \approx 0.135$, which is much closer to the value predicted by (4.5).

4.4. *Dynamics above the neutral curve*

The flow response for selected *Re* values was computed for $Ri \in [10^{-1}, 10^{1}]$ over at least four viscous times, and up to 15 viscous times for cases with low-frequency content. Responses associated with a coarse grid of logarithmically spaced *Ri* values were first obtained using zero velocity and a linear temperature profile as the initial condition. The responses for intermediate *Ri* were then obtained via continuation using these solutions as initial conditions. No systematic effort was made to identify multiple stable solutions, which do exist in certain parameter regimes (resulting in hysteresis), except in the subcritical band in the upper *Ri* range (the region shaded magenta in figures 2 and 13), where both the base state *S* and a time-dependent solution are stable and co-exist. In this region, a detailed investigation to find the edges of the hysteresis band was executed using a variety of different initial conditions.

An overview of the unsteady flow response over the extensive (*Ri*, *Re*) parameter regime considered is presented in figure 13, which provides, for each *Re* considered, the variation with *Ri* of the power spectral density (PSD) of the *E* time series. To obtain the individual PSDs, the *E* time series were first trimmed to remove transients, de-trended and Blackman filtered. The resulting PSDs were collated and normalised to peak power over all *Ri* values for each given *Re*. Table 1 contains the values of the normalising peak power of the PSD for each *Re* value, as well as the *Ri* value at the peaks. Since *E* already includes a scaling Re^2, these peak values merely represent the pre-factor for this scaling, and allow comparisons across different *Re*. Note that peak

https://doi.org/10.1017/jfm.2018.656 Published online by Cambridge University Press

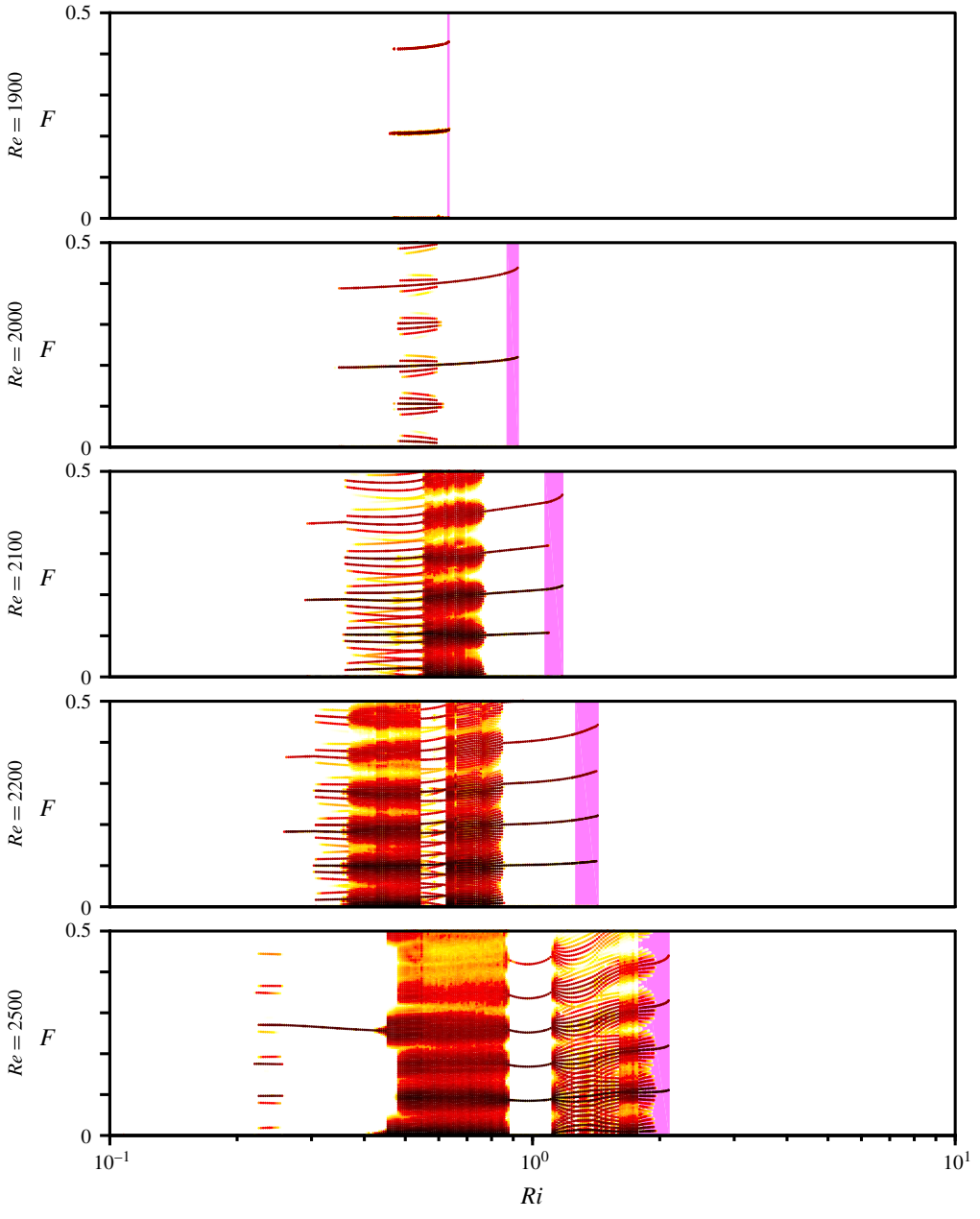


FIGURE 13. For caption see next page.

power is consistently reached at $Ri \approx 0.6$, i.e. when shear and buoyancy forces are of comparable strength. Figure 13 illustrates the increasing complexity of the responses as Re is increased. It shows a 'view from the top' of the normalised PSDs as a function of Ri obtained for each Re as indicated, with a colour scale from white (low energy) to red/black (high energy), corresponding to a power ratio of 10^5 (50 dB range). Values below 10^{-5} of peak power were omitted (set to white).

https://doi.org/10.1017/jfm.2018.656 Published online by Cambridge University Press

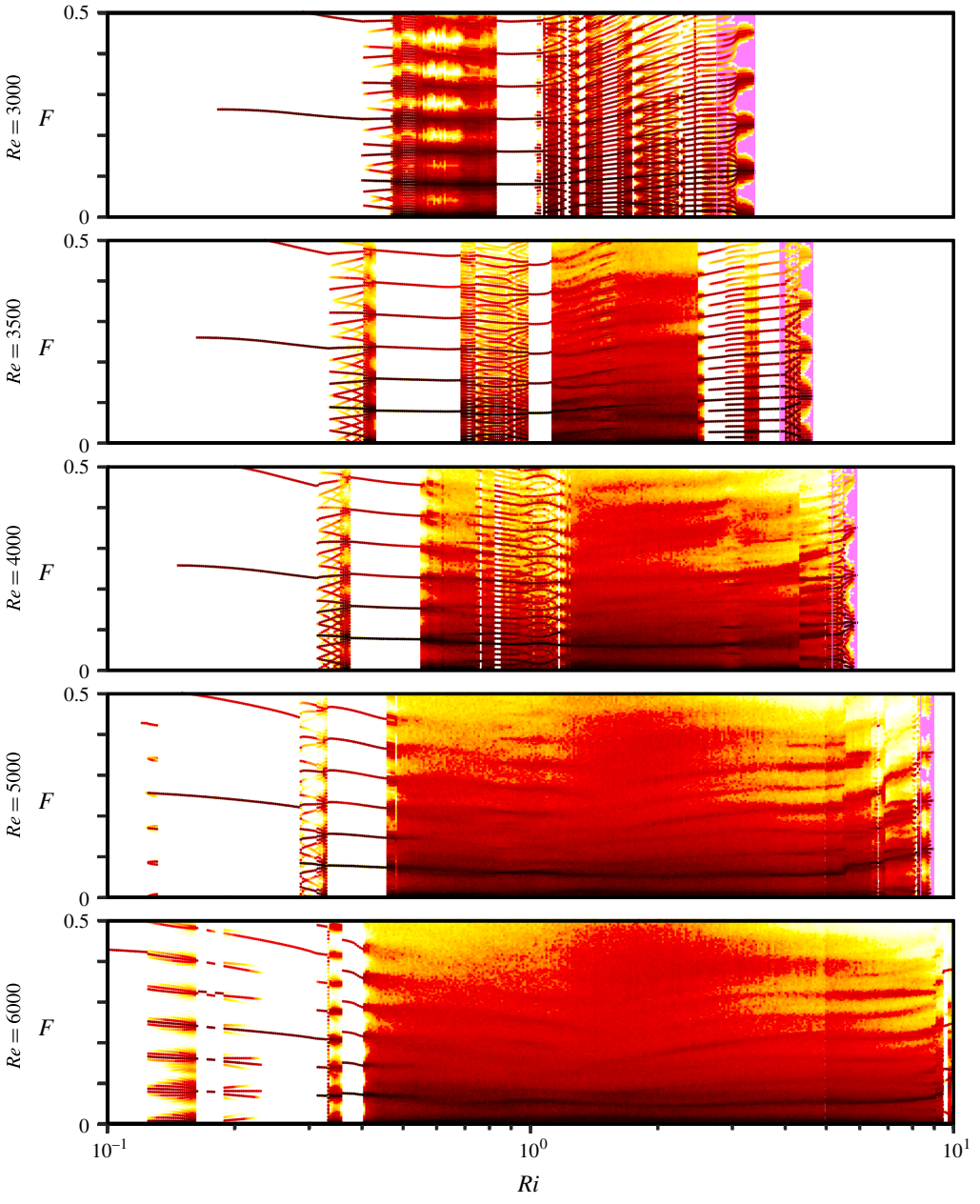


FIGURE 13 (cntd). (Colour online) Variation of the power spectrum density (PSD) of E with Ri, in terms of scaled frequency F, for Re as indicated. Black corresponds to peak energy at the given Re, and white is 50 dB or more below the peak.

As Re increases, the Ri band over which an unsteady response is obtained widens. At the lower Ri end of this range, the spectra is that of a pure limit cycle (single frequency plus harmonics), identified as L_2 for $Re \approx 1900$–2500, L_3 for $Re \approx 3000$–5000 and L_5 for $Re \approx 5000$ and 6000. At both $Re = 2500$ and $Re = 5000$, the respective limit cycles L_2 and L_5 quickly transform into quasi-periodic states, and then into limit

https://doi.org/10.1017/jfm.2018.656 Published online by Cambridge University Press

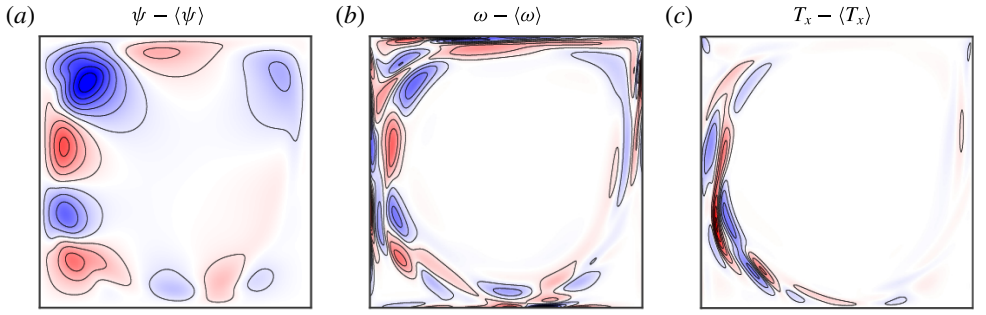


FIGURE 14. (Colour online) Snapshots of the deviations from their mean for streamfunction, vorticity and horizontal temperature gradient for the limit cycle L_4 at $Re = 6000$ and $Ri = 0.17$.

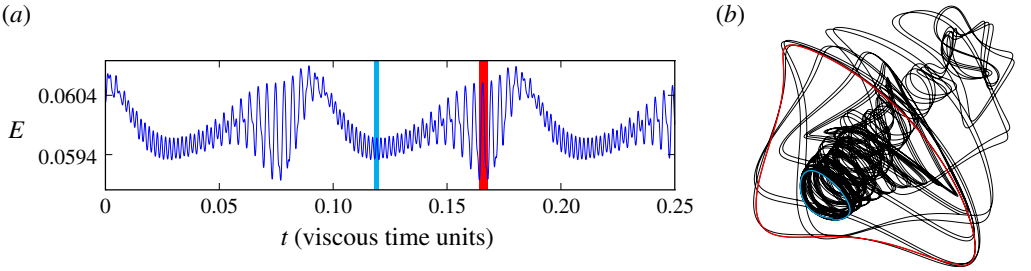


FIGURE 15. (Colour online) An example of global heteroclinic dynamics at $(Ri, Re) = (0.6902, 2100)$: (*a*) time series of the response E over a window of 0.25 viscous units and (*b*) corresponding phase portrait $(E(t-\tau), E(t))$ with delay $\tau = 1/(0.3Re\sqrt{1+Ri})$.

cycle L_3 as Ri increases across the Neimark–Sacker bifurcation curves emanating from the nearby double-Hopf points, dH_{23} and dH_{35}, described earlier. A pure limit cycle L_4 (figure 14), was also observed at $Re = 6000$ in a small range with $Ri \approx 0.17$, close to the supercritical Hopf bifurcation curve H_5, suggesting the presence of another Hopf bifurcation H_4. In the parameter regime considered, this Hopf bifurcation is not a primary instability of the basic state S. The scaled frequency of L_4 is $F \approx 0.325$, giving a rotation number $F/4 \approx 0.081$, which is comparable to those of the other limit cycles shown in figure 7(*b*).

With increasing Ri, the spectra of the computed responses become more complex showing characteristics typical of quasi-periodic flows with incommensurate frequencies. There are intervals in Ri where the spectra are periodic, due to the frequencies locking into rational ratios. These lockings are more prevalent at lower Re values. The locked regions (Arnol'd tongues) emerge from points along the Neimark–Sacker curves, which have their origin at the various double-Hopf points, and extend and interact far from the immediate vicinity of the double-Hopf points, leading to a panoply of more complex dynamical states featuring low-frequency spectral peaks associated with global homoclinic or heteroclinic behaviour (Boyland 1986).

An example of heteroclinic behaviour is presented in figure 15, which shows the E response at $Re = 2100$ and $Ri = 0.6902$. The time series (figure 15*a*) consists of a fast low-amplitude oscillation followed by a slower large-amplitude oscillation. This repeats periodically with a period of approximately 0.1 viscous time units. The short

https://doi.org/10.1017/jfm.2018.656 Published online by Cambridge University Press

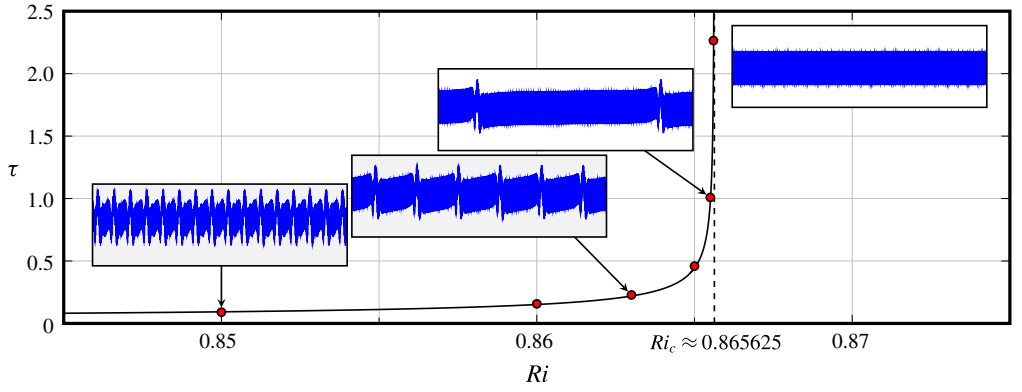


FIGURE 16. (Colour online) An example of homoclinic dynamics (SNIC on the torus) at $Re = 2750$ and $Ri \approx 0.86$: the quasi-period τ (in viscous time units) of a QP state (red bullets) and the black curve is the fit $\tau = 0.005 + 0.011/\sqrt{Ri_c - Ri}$, where Ri_c is the critical value of Ri at the SNIC bifurcation. The inserts show time series of $E \in [0.05, 0.06]$ over 1.4 viscous times at the indicated Ri. The time series for $Ri > Ri_c$ show the resulting locked response on the torus.

segments in the time series highlighted in blue and red correspond to times when the flow is close to the unstable (saddle) limit cycles L_2 and L_1. The nature of this near-heteroclinic cycle between the two saddle limit cycles is further illustrated in the phase portrait in figure 15(*b*), where the parts of the phase portrait corresponding to the blue and red segments of the time series are also coloured. These parts of the phase portrait have the same shape as the phase portraits of stable L_2 and L_1 limit cycles in figure 11(*a*,*c*). The rest of the phase portrait (in black) corresponds to the slow near-heteroclinic drift between the two limit cycles. These periodic drifts take approximately 0.05 viscous times, which is approximately 12 oscillations of L_1 and 24 oscillations of L_2.

An example of homoclinic behaviour is presented in figure 16, which shows the E response at $Re = 2750$ and selected values of $Ri \sim 0.86$. Below a critical value $Ri_c \approx 0.865625$ the response is a dyadic quasi-periodic state, with one scaled frequency that hardly varies with Ri, $F \approx 0.08$ (corresponding to a period of 0.033 viscous times), and a second lower frequency that goes to zero as $Ri \to Ri_c$. The corresponding period goes to infinity as $\tau = 0.005 + 0.011/\sqrt{Ri_c - Ri}$. The slow–fast behaviour seen in the time series terminates at $Ri = Ri_c$ with the creation of a pair of limit cycles on the torus, one unstable (saddle) and the other stable (node), at the saddle-node-on-an-invariant-cycle (SNIC) on a torus bifurcation (Lopez & Marques 2009). For $Ri > Ri_c$, only the stable limit cycle on the torus is observed via direct simulations.

Figure 17 presents snapshots of the horizontal temperature gradient T_x at $Re = 5000$ and four selected buoyancy strengths, $Ri = 2, 4, 6$ and 8. The four responses are quasi-periodic with a very low-frequency content (see figure 13). The snapshots are shown at a phase when the E oscillations are intense. The colour map is scaled by $3/Ri$, so that it is inversely proportional, at fixed Re, to the buoyancy intensity measured by the Grashof number Gr. With increasing Ri, the lid-driven roller is smaller and more confined to the upper downstream corner of the cavity. In all four cases, the relatively strong buoyancy pushes back on the roller quasi-periodically, and the shear forces exerted by the roller scoop up cold fluid from below and drive it up toward

https://doi.org/10.1017/jfm.2018.656 Published online by Cambridge University Press

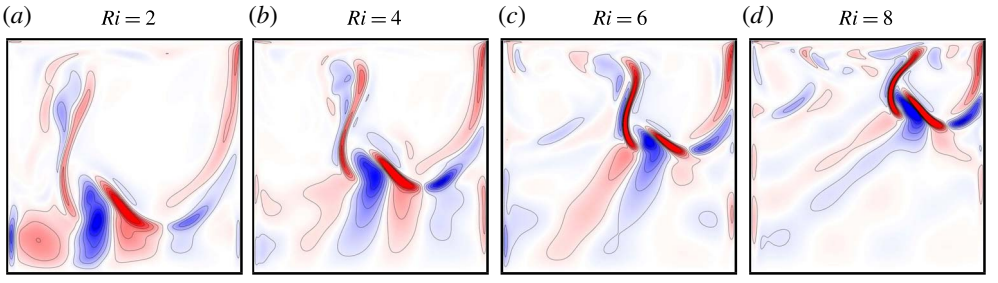


FIGURE 17. (Colour online) Snapshots of the horizontal temperature gradient T_x of quasi-periodic states at $Re = 5000$ and Ri as indicated; the contours are equispaced in the range $|T_x| \leqslant 3/Ri$. Supplementary movie 3 shows animations over 0.01 viscous time.

the hot lid. With increasing Ri, the colder fluid tends to impinge on the top lid and is alternately deflected to the right or to the left. In the latter case, this results in a wave of smaller (boomerang-shaped) cells propagating to the top upstream (left) corner of the cavity. This wave dissipates to some degree in the boundary layers but remains sufficiently strong so as to form a buoyancy barrier identifiable by the (blue, bean-shaped) stationary T_x cell evident in figures 17(*c*,*d*). This dynamics is more clearly evident in the accompanying supplementary movie 3.

Various flip bifurcations have also been detected above the neutral curve. Those occurring at $Re = 3500$ in the vicinity of $Ri = 3$ are relatively easy to identify in the PSDs shown in figure 13. For example, a frequency-locked limit cycle arising from a SNIC on the torus at $Ri \approx 2.57$ loses stability at $Ri \approx 2.63$ via a flip bifurcation, with the resulting period-doubled limit cycle itself losing stability via another flip bifurcation at $Ri \approx 2.86$. The period-quadrupled limit cycle remains stable up to $Ri \approx 3.2$. Beyond $Ri = 3.2$, the flow is aperiodic, and then frequency locks again at $Ri \approx 3.47$.

5. Conclusion

The impact of a stable temperature stratification on the flow of a fluid of Prandtl number $Pr = 1$ in a lid-driven square cavity was examined numerically over a comprehensive range of Reynolds numbers Re and Richardson numbers Ri quantifying the strengths of the shear and stratification, respectively. Particular attention was placed on how the competition between shear and stratification destabilises the flow and leads to complex dynamics.

At sufficiently small Re, the flow is steady and the results are in line with those from previous experimental studies in the square cavity (Koseff & Street 1985; Cohen *et al.* 2014): at lower Ri shear effects dominate and a large lid-driven roller occupies most of the cavity, while at larger Ri buoyancy effects confine the roller towards the downstream end of the top lid, leaving below a nearly stagnant linearly stratified fluid organised into a stack of weak counter-rotating horizontal cells driven by shears at the vertical walls.

For $Ri \lesssim 0.5$, the lid-driven roller drives hot fluid from the top of the cavity to interact with the colder fluid at the bottom, resulting in horizontal temperature gradients. These temperature gradients are sources of vorticity and combine with wall boundary layer effects to destabilise steady states at low Ri, compared to the isothermal case $Ri = 0$ at the same Re. The instability is a supercritical Hopf

https://doi.org/10.1017/jfm.2018.656 Published online by Cambridge University Press

bifurcation, and the instability mode (the Hopf eigenfunction) consists of m pairs of cells of opposite-signed vorticity (or horizontal temperature gradient) that propagate around the periphery of the roller. In the limit $Ri \to 0$, this matches the Hopf instability of the isothermal lid-driven cavity, with $m = 5$. For $0 < Ri < 0.5$, we find two more such supercritical Hopf bifurcations with $m = 3$ and 2, whose frequencies are related to an overall winding number m of the main roller.

For $Ri \gtrsim 0.5$, the instability of the steady flow switches to a subcritical Hopf, resulting in a hysteresis region where both the steady state and nonlinear unsteady states are attracting depending on initial conditions. At larger Ri this transition occurs at $Re \sim \sqrt{Ri}$. In that regime, the existence of a periodic limit cycle corresponding to a small roller with $m = 1$ confined to the downstream upper corner provides a localised periodic forcing which results in an internal wave beam propagating into the nearly linearly stratified fluid in the rest of the container. These waves are driven by the propagating cells on the periphery of the roller, with a frequency which adjusts to the buoyancy frequency so that the wave beams tend to propagate at 45° with increasing Ri. Indirect evidence of such internal wave beams was inferred from time series correlations in the experiments of Cohen *et al.* (2014).

Above the Hopf bifurcation curves, the various bifurcating modes interact nonlinearly and complicated dynamics ensue. The complexity increases with increasing Re; frequency spectra indicate the presence of quasi-periodic mixed modes with intervals of locking, as well as low-frequency responses due to homoclinic or heteroclinic dynamics. Even though the flow has multiple frequencies, and even a broadband spectrum in some parameter regimes, for large Ri since the roller is smaller and the lower region of the cavity is stratified (albeit nonlinearly), coherent wave beams triggered by the propagating cells along the periphery of the roller are still readily identifiable.

It is not clear to what extent three-dimensional effects, such as Taylor–Görtler vortices on the lid-driven roller, would affect the above described dynamics. It would be desirable to determine this. Cohen *et al.* (2014) report that the lid-driven stratified flow is not strongly three-dimensional in their experiments, and they were in parameter regimes comparable to those we have considered. Nevertheless, the two-dimensional results we present should be interpreted with some care. It is unfortunate that a comparably comprehensive parametric study in three dimensions is presently a daunting task.

Acknowledgements

This work was supported in part by the U.S. National Science Foundation grant CBET-1336410. The computations were performed on ASU research clusters as well as compute facilities in the School of Mathematical and Statistical Sciences.

Supplementary movies

Supplementary movies are available at https://doi.org/10.1017/jfm.2018.656.

REFERENCES

ANSONG, J. K. & SUTHERLAND, B. R. 2010 Internal gravity waves generated by convective plumes. *J. Fluid Mech.* **648**, 405–434.

AUTERI, F., PAROLINI, N. & QUARTAPELLE, L. 2002 Numerical investigation of the stability of singular driven cavity flow. *J. Comput. Phys.* **183**, 1–25.

https://doi.org/10.1017/jfm.2018.656 Published online by Cambridge University Press

BLANCHETTE, F., PEACOCK, T. & COUSIN, R. 2008 Stability of a stratified fluid with a vertically moving sidewall. *J. Fluid Mech.* **609**, 305–317.

BOYLAND, P. L. 1986 Bifurcations of circle maps: Arnol'd tongues, bistability and rotation intervals. *Commun. Math. Phys.* **106**, 353–381.

BREZILLON, A., GIRAULT, G. & CADOU, J. M. 2010 A numerical algorithm coupling a bifurcating indicator and a direct method for the computation of Hopf bifurcation points in fluid mechanics. *Comput. Fluids* **39**, 1226–1240.

CHENG, T. S. & LIU, W.-H. 2010 Effect of temperature gradient orientation on the characteristics of mixed convection flow in a lid-driven square cavity. *Comput. Fluids* **39**, 965–978.

COHEN, N., EIDELMAN, A., ELPERIN, T., KLEERIN, N. & ROGACHEVSKII, I. 2014 Sheared stably stratified turbulence and large-scale waves in a lid driven cavity. *Phys. Fluids* **26**, 105106.

DOHAN, K. & SUTHERLAND, B. R. 2003 Internal waves generated from a turbulent mixed region. *Phys. Fluids* **15**, 488–498.

FERNANDO, H. J. S. 1991 Turbulent mixing in stratified fluids. *Annu. Rev. Fluid Mech.* **23**, 455–493.

FORTIN, A., JARDAK, M., GERVAIS, J. J. & PIERRE, R. 1997 Localization of Hopf bifurcations in fluid flow problems. *Intl J. Numer. Meth. Fluids* **24**, 1185–1210.

HANRATTY, T. J., ROSEN, E. M. & KABEL, R. L. 1958 Effect of heat transfer on flow field at low Reynolds numbers in vertical tubes. *Ind. Engng Chem.* **50**, 815–818.

HUGUES, S. & RANDRIAMAMPIANINA, A. 1998 An improved projection scheme applied to pseudospectral methods for the incompressible Navier–Stokes equations. *Intl J. Numer. Meth. Fluids* **28**, 501–521.

IVEY, G. N., WINTERS, K. B. & KOSEFF, J. R. 2008 Density stratification, turbulence, but how much mixing? *Annu. Rev. Fluid Mech.* **40**, 169–184.

IWATSU, R., HYUN, J. H. & KUWAHARA, K. 1993 Mixed convection in a driven cavity with a stable vertical temperature gradient. *Intl J. Heat Mass Transfer* **36**, 1601–1608.

JI, T. H., KIM, S. Y. & HYUN, J. M. 2007 Transient mixed convection in an enclosure driven by a sliding lid. *Heat Mass Transfer* **43**, 629–638.

KNOBLOCH, E. & PROCTOR, M. R. E. 1988 The double Hopf bifurcation with 2 : 1 resonance. *Proc. R. Soc. Lond.* A **415**, 61–90.

KOSEFF, J. R. & STREET, R. L. 1985 Circulation structure in a stratified cavity flow. *J. Hydraul. Engng* **111**, 334–354.

KUZNETSOV, Y. A. 2004 *Elements of Applied Bifurcation Theory*, 3rd edn. Springer.

LOPEZ, J. M. & MARQUES, F. 2009 Centrifugal effects in rotating convection: nonlinear dynamics. *J. Fluid Mech.* **628**, 269–297.

LOPEZ, J. M., WELFERT, B. D., WU, K. & YALIM, J. 2017 Transition to complex dynamics in the cubic lid-driven cavity. *Phys. Rev. Fluids* **2**, 07441.

MAITI, M. K., GUPTA, A. S. & BHATTACHARYYA, S. 2008 Stable/unstable stratification in thermosolutal convection in a square cavity. *Trans. ASME J. Heat Transfer* **130**, 122001.

MAJDA, A. J. & SHEFTER, M. G. 1998 Elementary stratified flows with instability at large Richardson number. *J. Fluid Mech.* **376**, 319–350.

MAJDA, A. J. & SHEFTER, M. G. 2000 Nonlinear instability of elementary stratified flows at large Richardson number. *Chaos* **10**, 3–27.

MICHAELIAN, M. E., MAXWORTHY, T. & REDEKOPP, L. G. 2002 The coupling between turbulent, penetrative convection and internal waves. *Eur. J. Mech. (*B*/Fluids)* **21**, 1–28.

MUNROE, J. R. & SUTHERLAND, B. R. 2014 Internal wave energy radiated from a turbulent mixed layer. *Phys. Fluids* **26**, 096604.

NICOLÁS, A. & BERMÚDEZ, B. 2005 2D thermal/isothermal incompressible viscous flows. *Intl J. Numer. Meth. Fluids* **48**, 349–366.

PELTIER, W. R. & CAULFIELD, C. P. 2003 Mixing efficiency in stratified shear flows. *Annu. Rev. Fluid Mech.* **35**, 135–167.

PHAM, H. T., SARKAR, S. & BRUCKER, K. A. 2009 Dynamics of a stratified shear layer above a region of uniform stratification. *J. Fluid Mech.* **630**, 191–223.

POLIASHENKO, M. & AIDUN, C. K. 1995 A direct method for computation of simple bifurcations. *J. Comput. Phys.* **121**, 246–260.

https://doi.org/10.1017/jfm.2018.656 Published online by Cambridge University Press

SHERMAN, F. S., IMBERGER, J. & CORCOS, G. M. 1978 Turbulence and mixing in stably stratified waters. *Annu. Rev. Fluid Mech.* **10**, 267–288.

STEVENS, C. & IMBERGER, J. 1996 The initial response of a stratified lake to a surface shear stress. *J. Fluid Mech.* **312**, 39–66.

TURNER, J. S. 1979 *Buoyancy Effects in Fluids*. Cambridge University Press.

VANEL, J.-M., PEYRET, R. & BONTOUX, P. 1986 A pseudo-spectral solution of vorticity-stream function equations using the influence matrix technique. In *Numerical Methods for Fluid Dynamics II* (ed. K. W. Morton & M. J. Baines), pp. 463–475. Clarendon Press.

https://doi.org/10.1017/jfm.2018.656 Published online by Cambridge University Press